Research

Polarized iridescence of the multilayered elytra of the Japanese jewel beetle, *Chrysochroa fulgidissima*

Doekele G. Stavenga[1], Bodo D. Wilts[1,2,*], Hein L. Leertouwer[1] and Takahiko Hariyama[3]

[1]*Department of Neurobiophysics, and* [2]*Department of Applied Physics, Zernike Institute for Advanced Materials, University of Groningen, Nijenborgh 4, 9747 AG Groningen, The Netherlands*
[3]*Laboratory of Biology, Hamamatsu University School of Medicine, 1-20-1 Handayama, Hamamatsu 431-3192, Japan*

The elytra of the Japanese jewel beetle *Chrysochroa fulgidissima* are metallic green with purple stripes. Scanning electron microscopy and atomic force microscopy demonstrated that the elytral surface is approximately flat. The accordingly specular green and purple areas have, with normal illumination, 100–150 nm broad reflectance bands, peaking at about 530 and 700 nm. The bands shift progressively towards shorter wavelengths with increasing oblique illumination, and the reflection then becomes highly polarized. Transmission electron microscopy revealed that the epicuticle of the green and purple areas consists of stacks of 16 and 12 layers, respectively. Assuming gradient refractive index values of the layers between 1.6 and 1.7 and applying the classical multilayer theory allowed modelling of the measured polarization- and angle-dependent reflectance spectra. The extreme polarized iridescence exhibited by the elytra of the jewel beetle may have a function in intraspecific recognition.

Keywords: multilayer theory; melanin; Buprestidae; camouflage; polarization

1. INTRODUCTION

Structural colours created by multilayers are widely used in the animal kingdom for display and/or camouflage [1–3]. Striking examples are the jewel beetles, woodboring beetles of the Buprestidae family, which display resplendent metallic colours owing to multilayers in the cuticle [4]. For *Euchroma gigantea*, the ceiba borer beetle, Durrer & Villiger [5] concluded that the epicuticle consists of a stack of five melanin-containing layers, 60–80 nm thick and embedded at a regular distance of 60 nm in chitin. Similar layered structures have been demonstrated to exist in other Buprestidae, e.g. the jewel beetles *Chrysochroa vittata* [6,7], *Chrysochroa fulgidissima* [8,9] and *Chrysochroa raja* [10].

The Japanese jewel beetle, *C. fulgidissima*, has beautiful, brilliant green elytra with longitudinal purplish stripes. Because of their striking iridescence, this jewel beetle was used as ornament in ancient Japanese times. Indeed, its Japanese name, Tamamushi-no-zushi, derives from archaic Japanese 'Tama', meaning jewels or beautiful things and 'Mushi', meaning small animals. The famous seventh century Japanese national treasure Tamamushi-no-zushi, the beetle wing shrine, was decorated with innumerous iridescent elytra of *C. fulgidissima*.

Previous optical studies of the iridescence of jewel beetles have attempted to establish a quantitative description of measured reflectance spectra using multilayer modelling [8,10] and furthermore have shown that the beetles' photonic structures can inspire biomimetic applications [6]. Here, we extend the previous work by presenting a comprehensive set of reflectance spectra, measured as a function of angle and polarization. By using various optical approaches, among others a novel imaging scatterometer (ISM) [11], we establish that the epicuticle of the beetle's elytra can be well treated as an ideal multilayer interference reflector that creates a strong polarized iridescence. We show that a classical multilayer with a gradient refractive index is an appropriate model for the jewel beetle elytra, providing an in-depth understanding of the *Chrysochroa* beetle's coloration. The range of the refractive index gradient realized in the jewel beetle cuticle appears to be surprisingly narrow.

2. MATERIAL AND METHODS
(a) *Animals*
Chrysochroa fulgidissima specimens were collected at the campus of the Hamamatsu University School of Medicine, in Shizuoka Prefecture, Japan, from June to August 2004.
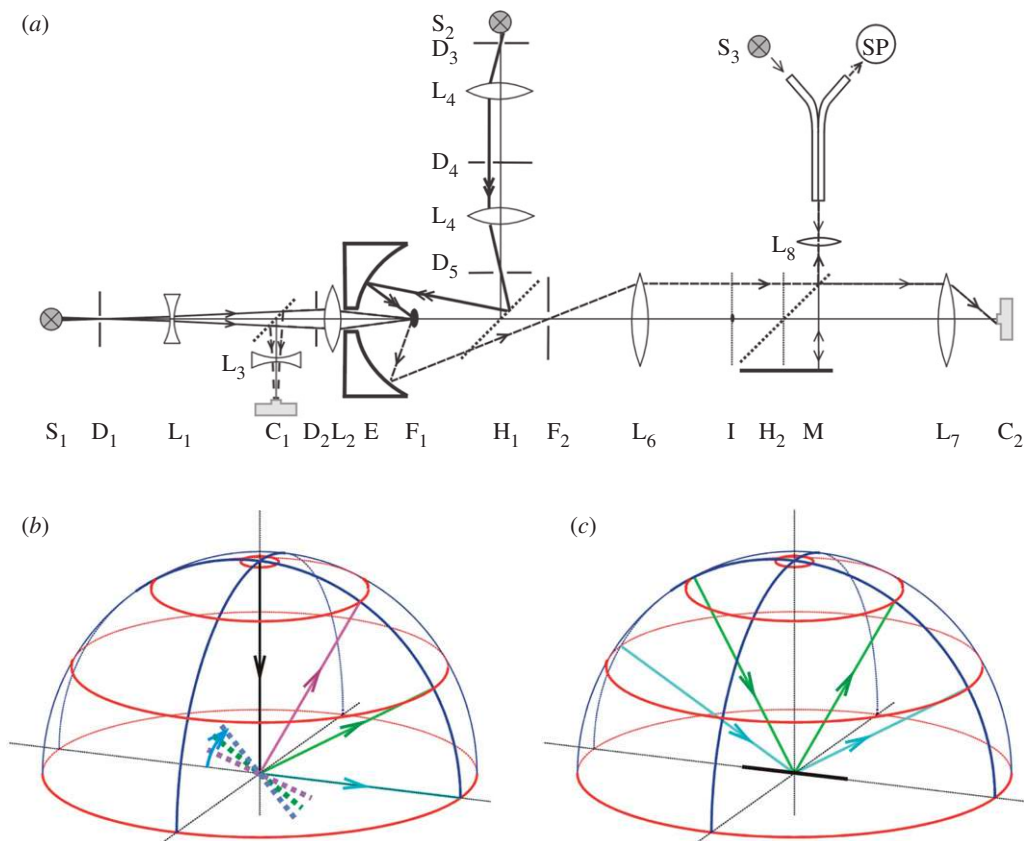
* Author for correspondence (b.d.wilts@rug.nl).

Figure 1. Imaging scatterometry. (*a*) Diagram of the imaging scatterometer. The primary light beam is delivered by light source S_1 and the secondary beam by S_2. Cameras C_1 and C_2 document the near-field and far-field scattering by the object, located in the focal plane F_1 of an ellipsoidal mirror (E); see further §2. (*b*) When the object is specular and rotated over angles of 15°, 30° and 45°, then light from the axial, primary beam (black ray) is reflected by the object in angular directions of 30° (magenta), 60° (green) and 90° (cyan). (*c*) Light from the secondary beam reaching a specular object from an angle of incidence of 30° (green) or 60° (cyan) is reflected in the opposite angular direction. Generally, light will be scattered by the object in a wide range of spatial angles (as indicated by the dashed ray in (*a*)).

(b) *Anatomy*

The elytra were removed from the body, using a razor blade and fine scissors, for studying their anatomy. Details of the elytral surface were photographed with an Olympus SZX16 stereomicroscope equipped with an Olympus DP70 digital camera, and with a Philips XL-30 ESEM scanning electron microscope (SEM).

The elytral surface was scanned with a Veeco Dimension 3100 atomic force microscope (AFM), used in dynamic mode with Olympus AC240TS tips with tip radius less than 7 nm.

For transmission electron microscopy (TEM), the elytra were immersed in primary fixative solution (2.5% glutaraldehyde, 2.5% paraformaldehyde in 0.1 M phosphate buffer, pH = 7.4) and placed for 12 h in a refrigerator at 4°C. Tissues were rinsed several times in phosphate buffer solution, post-fixed for 2 h with 1 per cent OsO_4 in the same buffer at room temperature, dehydrated through a graded series of ethanol solutions and after transfer to propylene oxide embedded in a mixed solution of Epon 812 (TAAB) and Araldite (TAAB). Dehydration effects of the dry cuticle were assumed to be of minor size. Sections were cut with an ultramicrotome and picked up with 100-mesh copper grids. The sections were double-stained with 2 per cent uranyl acetate and 0.4 per cent lead citrate solution for 5 and 3 min, respectively, and observed with a

JEM-1220 (JEOL) transmission electron microscope at 80 kV emission voltage.

Using MATLAB, the TEM micrographs revealing the multilayer in the epicuticle were evaluated by determining the average value of the image pixels in 10 nm thick layers, $I(z)$, where z is the coordinate perpendicular to the cuticle surface. Subsequently, the optical density, $D(z) = -\log_{10}[I(z)]$, was calculated, assuming that the density is proportional to the concentration of electron-dense material.

(c) *Imaging scatterometry and spectrometry*

The spatial distribution of the light scattered by the elytra was visualized with an ISM, a diagram of which is shown in figure 1*a*. A small piece of an elytron was therefore glued to a tip of a glass micropipette. The wing piece, the object, was positioned in the first focal plane (F_1) of an elliptical mirror (E), where it was viewed and photographed via a small, about 5°, axial hole in the mirror with camera C_1 (Jenoptik ProgRes C10). The object was illuminated with the primary beam, delivered by light source S_1 via diaphragms $D_{1,2}$ and lenses $L_{1,2}$, and/or by the secondary beam, from light source S_2 via diaphragms D_{3-5}, lenses $L_{4,5}$ and half-mirror H_1. The light scattered by the object into the frontal hemisphere was focused by the elliptical mirror in its second focal
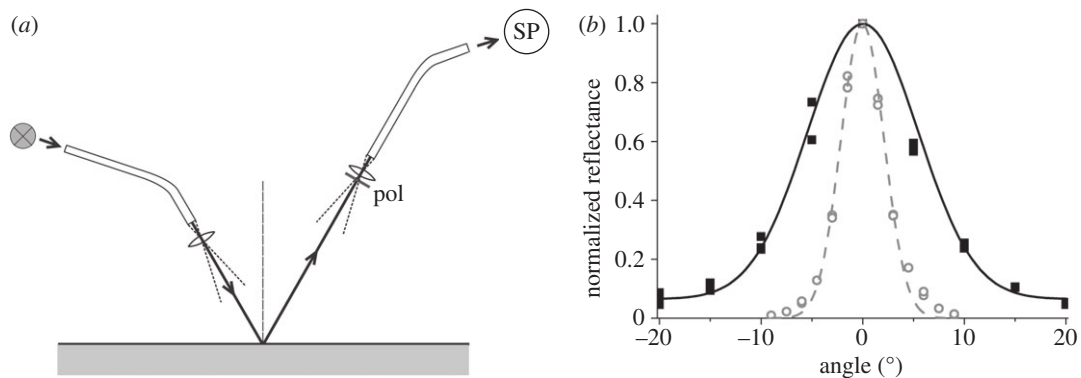
Figure 2. Polarization- and angle-dependent spectrometry. (*a*) The left-hand rotatable optical fibre, equipped with a lens, channels incident light onto the object and the right-hand rotatable optical fibre captures the scattered light and channels it to a spectrometer (SP). (*b*) The angular spread of the light reflected from a mirror and beetle cuticle have half-widths of about 5° and 12°, respectively. Filled squares with solid line, beetle; open circles with dashed line, mirror.

plane, F_2, and imaged by lens L_6 in its back focal plane, I, which thus received the object's spatial distribution of scattered light. An opaque object positioned axially in plane I served as a spatial filter, blocking the transmitted light from the primary beam. The scattered light pattern of plane I was imaged by lens L_7 onto camera C_2 (Olympus DP70). The images, corrected for the optical distortions of the set-up, were converted into polar plots (figure 5). Figure 1*b* diagrammatically shows how light from the axial primary beam is reflected by a specular object rotated in steps of 15°, from 0° to 45°, and figure 1*c* diagrammatically shows how light from the secondary beam with angles of incidence 30° and 60° is reflected by a specular object, normal to the axis of the scatterometer. The red circles in the hemispheres of figure 1*b*,*c* indicate angular directions of 5°, 30°, 60° and 90°, which are also drawn in the polar plots.

The set-up shown in figure 1*a* is a slight modification of that described by Stavenga *et al.* ([11]; see also [12,13]). The added facility, a CCD detector array spectrometer (SP; AvaSpec-2048-2, Avantes, Eerbeek, The Netherlands), samples a small area of the scattered light pattern via half-mirror H_2, lens L_8 and one channel of a bifurcated light guide (effective aperture approx. 4°). The other channel of the bifurcated light guide was connected to a source S_3, the light of which was focused by L_8 onto mirror M, which is conjugated to plane I by half-mirror H_2. The light beam reflected by mirror M and subsequently reflected by H_2 towards lens L_7 reached camera C_2, and thus allowed identification of the area sampled by spectrometer. Laterally displacing the fibre tip together with lens L_8 allowed sampling of any area of choice of the scattering pattern in plane I, and hence of any chosen spatial direction of the light scattered by the object. A small piece of MgO served as a white diffusing reference object. The differences in spatial scattering profiles of the object and reference were accounted for in the calculations of the reflectance spectra.

The reflectance spectra of small elytral areas were measured with a microspectrophotometer (MSP), consisting of a xenon light source, a Leitz Ortholux microscope and an S2000 fibre optic spectrometer (Ocean Optics). The microscope objective was an Olympus 20×, NA 0.46.

(d) Polarization- and angle-dependent reflectance measurements

The polarization and angle dependence of the reflectance spectra of the elytra were measured by using two optical fibres (figure 2*a*). One end of the first optical fibre was connected to a deuterium/halogen light source (AvaLight-D(H)-S) or a xenon lamp, and its other end was mounted on a goniometer together with a small lens, which focused the fibre tip at the goniometer's rotation axis. The second fibre was mounted with one end at a second goniometer, together with a similarly focusing lens and a polarization filter that could be rotated around the optical axis of lens and fibre entrance; the other end was connected to a CCD detector array spectrometer (AvaSpec-2048-2). The rotation axes of the two goniometers coincided and the two fibres rotated in the same plane. The patch to be measured was positioned in that plane, at the axis of rotation of the goniometers. The aperture of the fibres was 5° (full width at half maximum, FWHM) and the distance of the tips to the centre of the illuminated spot was 4 and 12 cm, respectively. The receiving fibre thus sampled a larger area than the illuminated spot, but it did not fully capture all the reflected light. The spatial reflectance profile of a mirror illuminated with a static illumination fibre and measured with a rotating receiving fibre was approximately Gaussian, with aperture 5° (FWHM; figure 2*b*). The beetle cuticle approximated an ideal reflector; the aperture of the reflected light was 12° (FWHM), independent of the angle of light incidence (figure 2*b*). Therefore, at all illumination angles, the same fraction of the reflected light was captured. In the reflectance measurements, a white diffusing reference tile (Avantes WS-2) served as reference. The reflectance spectra were corrected for the difference in spatial scattering properties of the object and reference.

(e) Modelling

The reflectance of the multilayer in the epicuticle of the jewel beetles' elytra was calculated by applying the classical multilayer theory for dielectric media (see the appendix). Both the real (n) and imaginary (k) part of the refractive index of the cuticle were
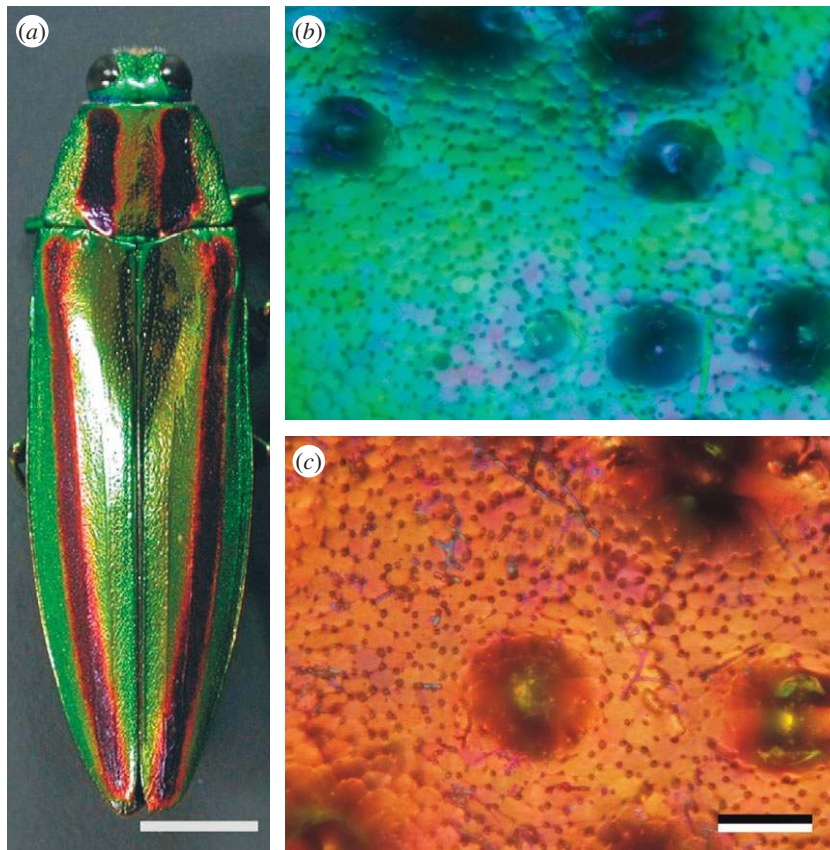
Figure 3. (a) Dorsal view of a female Japanese jewel beetle, *Chrysochroa fulgidissima*. The elytra and thorax are green with purple stripes (scale bar, 0.5 cm). (*b,c*) Details of the elytra. The surface of both the green (*b*) and purple (*c*) cuticle has a number of large pits and numerous small indentations, marking a tessellated surface pattern (scale bar, 100 μm).
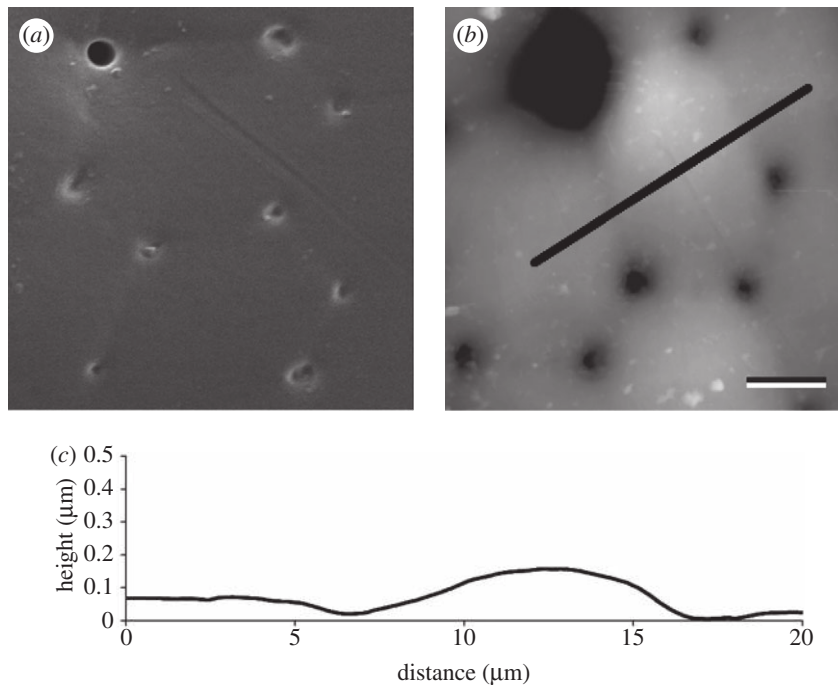

Figure 4. (*a*) SEM and (*b*) AFM of the elytral surface (scale bar, 5 μm). (*c*) Height profile of the surface along the green line of (*b*) (note that the abscissa-ordinate aspect ratio is 10 : 1).

assumed to be proportional to the optical density derived from the TEM micrographs: $n(z) = 1.58 + aD(z)$ and $k(z, \lambda) = b\ \kappa(\lambda)D(z)$, with $a = 0.15$ and $b = 1$ for the green area, and $a = 0.1$ and $b = 2$ for the purple area, with $\kappa(\lambda) = (\lambda/4\pi)*\alpha(\lambda)$ and $\alpha(\lambda)$ the absorption spectrum for melanin, determined from transmission measurements, normalized at 500 nm (the dimension of α is μm^{-1} when taking λ

in μm; see figure 11*a*). The parameters *a* and *b* were determined heuristically to optimize agreement between the model and the experiment.

3. RESULTS

(a) *Optical properties*

The Japanese jewel beetle, *C. fulgidissima*, has a brightly reflecting cuticle in virtually all body parts. The elytra, which mainly determine the beetles' appearance when at rest, reflect maximally in the green region, with longitudinal, dark-purple stripes interrupting the pattern; at the borders in between the green and purple areas, the cuticle is red/orange (figure 3*a*). The female and male are coloured almost identically, and the only apparent difference between the two sexes is that the males have more prominent eyes [8]. Observing the elytra at higher magnification reveals that the colour of the elytral surface is not unique and can vary between yellow and violet in the green region (figure 3*b*) and from orange to deep red/purple in the purple region (figure 3*c*). This indicates that locally the multilayers below the surface, which cause the colour, can slightly vary in layer thickness and/or refractive index.

The elytral surface is dotted with distinct pits having distances about 100 μm together with numerous minor indentations, with distances of the order of 10 μm (figure 3*b,c*), which form a tessellated pattern of more or less hexagonal tiles. The irregular surface will affect the reflection properties, and therefore we investigated the elytral surface with scanning electron microscopy (figure 4*a*) and atomic force microscopy (figure 4*b,c*). The surface in between the minor indentations appeared to be indeed not flat, but the radius of curvature of the tiles is rather large, about 100 μm (figure 4*b*), so that the normal to the surface changes over no more than approximately $6-7°$. Over a large area, the direction of the normal to the surface will vary more, of course, especially near the pits and indentations, but the latter structures make up only a minor part of the surface, and therefore we conclude that in fair approximation the elytra will locally act as approximately plane reflectors.

(b) *Imaging scatterometry*

That the elytra act as plane reflectors was confirmed with the ISM of figure 1*a*. Small pieces of the green as well as purple elytral areas were mounted in the scatterometer and, using the white light primary beam (S_1) with a small diaphragm (D_1), an area with diameter 40 μm was illuminated (indicated by the circle in figure 5*a,b*). The illuminated area appeared as dotted (figure 5*a,b*), with each dot representing a tile of the tessellated cuticle, because the aperture of the primary beam as well as that of the near-field (nf) camera C_1 (figure 1*a*) are limited to 5° [11], and thus the scattered light from the rims of the tiles could not be captured by the camera. The scattering of the illuminated elytral piece was investigated in four cases where the angle of incidence was 0°, 15°, 30° and 45°, respectively. This was realized by rotating the elytral pieces around an axis perpendicular to the direction of illumination in steps of 15° as indicated
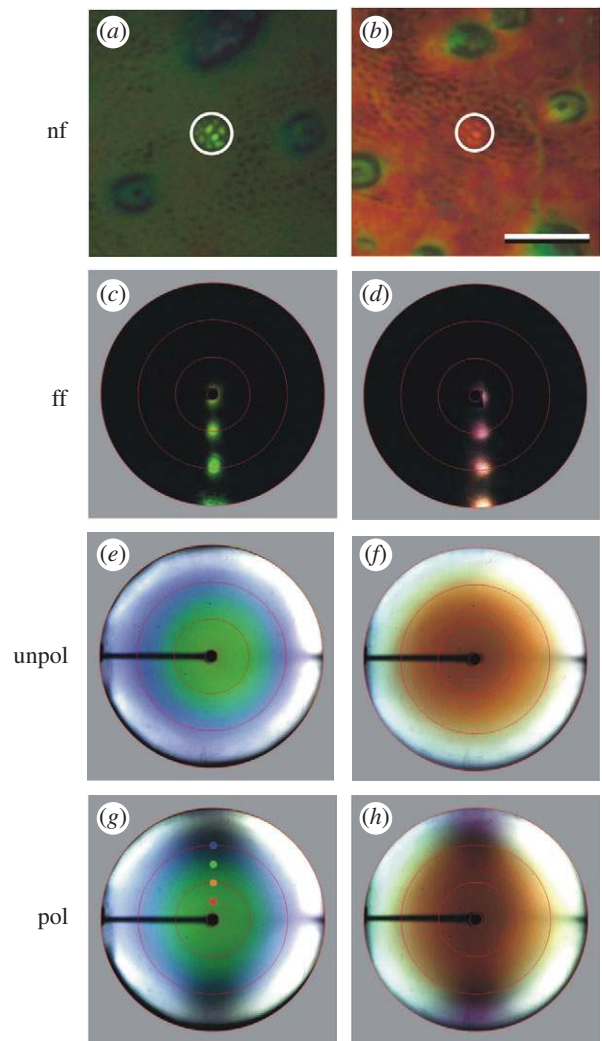

Figure 5. Imaging scatterometry of (*a,c,e,g*) green and (*b,d,f,h*) purple elytral areas ((*b*) scale bar, 100 μm). The near-field (nf; *a,b*) photographs show the illumination of a small area, diameter about 40 μm, with the primary beam. (*c,d*) Rotating the elytral piece over angles of 15°, 30° and 45° yields narrow reflection beams with direction angles of 30°, 60° and 90°, respectively (compare diagram figure 1*b*). Wide-aperture illumination yields scattering patterns that are (*e*) green and (*f*) brown purple in the centre and white at large angles when using unpolarized (unpol) light (compare diagram figure 1*c*). (*g,h*) With vertically linearly polarized (pol) light, the reflection appears to vanish for large angles of incidence, around a plane parallel to the polarization of the illumination. The red, orange, green and blue dots in (*g*) indicate the directions of reflection (and illumination) of 15°, 30°, 45° and 60° investigated in figure 6.

in figure 1*b*. The resulting scattering patterns, documented by the far-field (ff) camera C_2 (figure 1*a*) are shown superimposed in figure 5*c* (green) and *d* (purple). For both the green and the purple elytra, the scattering patterns were directionally very restricted spots, with half-width of the spatial profile about 10°, centred around the directional angles 0°, 30°, 60° and 90° (as expected for an ideal mirror; the central reflection spot, representing reflection on the surface oriented perpendicularly to the illuminating beam, is incomplete, because of the 10° central black hole in the elliptical mirror and the blocking spatial filter in plane I; figure 1*a*).
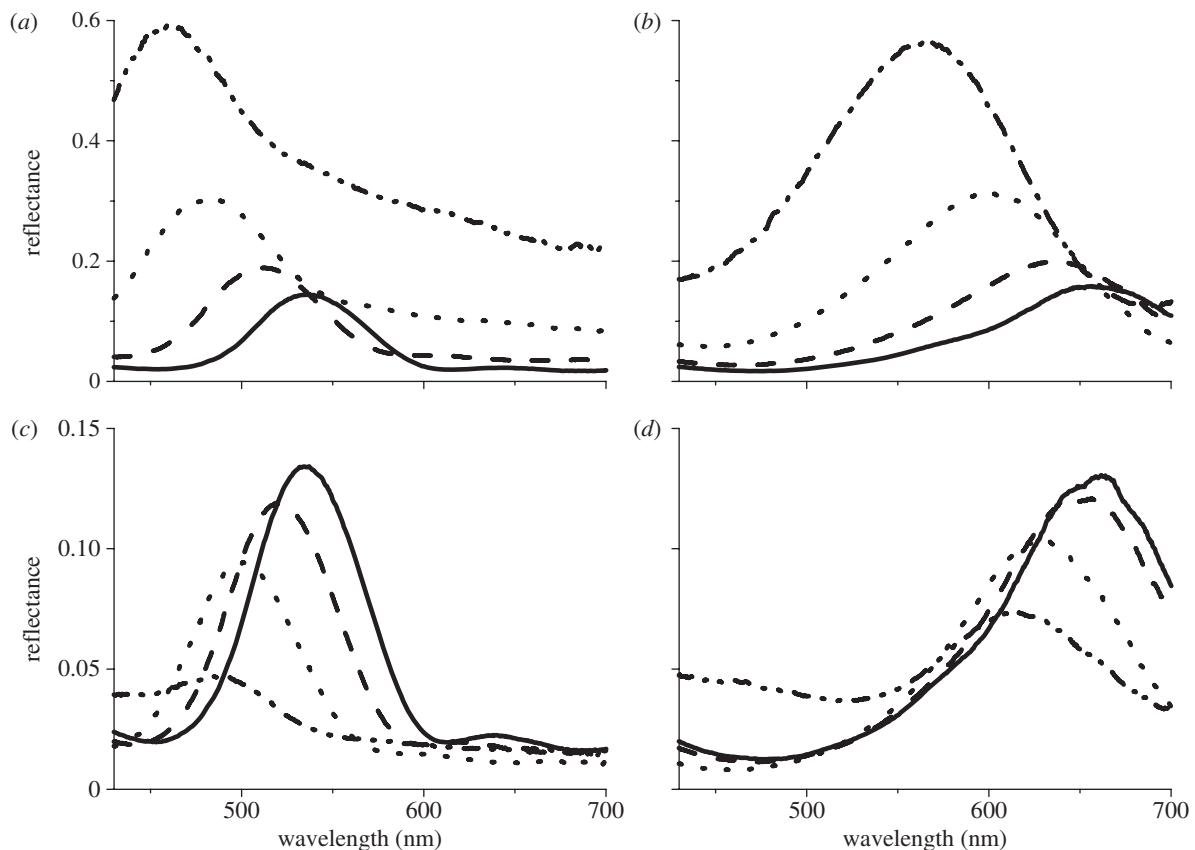
Figure 6. Reflectance spectra of the (*a*,*c*) green and (*b*,*d*) purple elytral pieces for a few angular directions, measured with the spectrometer section of the imaging scatterometer (figure 1*a*). The angular directions (15°, 30°, 45° and 60°) were in the vertical plane of the scattering pattern (figure 5*g*), with the light vector perpendicular (TE; *a*,*b*) and parallel (TM; *c*,*d*) to the (vertical) plane of light incidence. The TE- and TM-reflectance shifted hypsochromically with increasing angle of incidence and reflection, for both the green and purple elytra. The TE reflectance increased in amplitude, but the TM reflectance decreased in amplitude. Solid lines, 15°; dashed lines, 30°; dotted lines, 45°; dashed dotted lines, 60°.

The beetle's cuticle is of course not an ideal mirror, but a multilayer reflector, as witnessed by the dependence of the colour of the reflected spots on the angle of illumination. Illumination of the cuticle with a white, wide-aperture beam should therefore result in a variety of colours. A wide-aperture illumination was realized with the secondary beam (see the diagram in figure 1*c*) by completely opening up (i.e. removing) diaphragm D_4 (figure 1*a*). With unpolarized light, a green elytron reflects green into angles up to about 45°, which changes at larger angles into blue and violet, and at angles above 70°, a broad-band white reflection results (figure 5*e*). The angular scattering pattern is virtually circular and symmetrical, except for the black bar at 180° of the polar diagram, which is due to the pipette holding the elytral piece obstructing the light reflected by the elliptical mirror. The purple elytral piece reflects dark-red/brown into angles up to about 30°, changing into red/orange at angles around 60°, and into yellow and broad-band white above an angle of incidence and reflection of 60° (figure 5*f*). We emphasize here that figure 5*e*,*f* demonstrates that the ISM in a single picture captures the angle dependence of the colour of the reflected light.

It is well known that multilayer reflectance not only depends on the angle of illumination, but also on the degree of polarization [14–16]. We therefore inserted a (vertically) polarizing filter into the white illumination beam. This results in dark areas in the scatterograms (figure 5*g*,*h*), apparently because the polarized light is poorly reflected in certain angular directions. Upon rotation of the polarization filter, the patterns of figure 5*g*,*h* rotated simultaneously, demonstrating the rotational symmetry of the elytral scattering.

The angle-dependent reflection of the polarized light was studied in more detail with the spectrometer attachment of our scatterometer (figure 1*a*). The spectra for both TE- (transverse electric or s-) and TM- (transverse magnetic or p-) polarized light were obtained for a few different angular directions (15°, 30°, 45° and 60°) in the vertical plane of the scattering pattern (figure 6). The TE- and TM-reflectance bands shifted hypsochromically for both the green and purple elytra (figure 6*a*,*b*). The TE reflectance increased in amplitude, but the TM reflectance decreased in amplitude (figure 6*c*,*d*).

(c) *Polarization- and angle-dependent spectrometry*

For detailed spectrometry, especially concerning the angle dependence of the polarization, the set-up with two rotating fibres, diagrammatically shown in figure 2*a*, appeared to be more flexible than the scatterometer. Small spots of the green and purple areas of the

elytra were illuminated with focused white light from one fibre and the reflected light was collected by the second fibre, which was equipped with a polarizing filter. With about normal illumination, the reflectance spectra obtained from various areas showed a distinct band, peaking at 500–550 nm (green) or 650–720 nm (purple), with half-width approximately 100 (green) and approximately 150 nm (purple). As to be expected from the scattering patterns of figure 5, the reflectance spectra strongly depended on the angle of light incidence. We changed the angle of light incidence, θ_0, in steps of 10° when $\theta_0 < 50°$ and in steps of 5° when $\theta_0 > 50°$, and simultaneously changed the angle of the measurement fibre, symmetrical with respect to the normal to the elytral surface. It thus appeared again that for both TE- and TM-polarized light, the peak wavelength shifted to shorter wavelengths (figure 7a–f). For TE-polarized light, the peak reflectance increased with an increasing angle of incidence, for both the green and purple areas (figure 7g,h), but for TM-polarized light, the peak reflectance decreased, becoming minimal at an angle of incidence of approximately 65–70°; at larger angles, the overall spectral reflectance increased again (figure 7c,d), but at the wavelengths where the TE-polarized light had a peak, the TM light then featured a trough (figure 7g,h).

(d) *Anatomy*
The observed polarization-dependent phenomena are quite characteristic for a multilayer. To interpret the angle-dependent reflectance spectra quantitatively, the thicknesses of the layers and the values of the refractive indices have to be known. The multilayer thicknesses were obtained by TEM of pieces of cuticle from the green (figure 8a) and purple (figure 8b) areas. In both cases, an about 1.3 μm thick distal sheet, forming the epicuticle, features several layers with alternating high and low electron density, about 16 in the green area and about 12 in the purple area. The more proximal exocuticle is approximately uniformly stained. The electron density is presumably related to the refractive index of the material that creates the light-reflecting multilayer. The average density of the images calculated in 10 nm thick slabs parallel to the surface appeared to oscillate more or less sinusoidally as a function of depth, with oscillation periods about 160 and 205 nm for the green and purple areas, respectively (figure 8c).

The transmission electron micrographs are of course from a very local area and not necessarily representative for all areas of the elytra cuticle. To assess the variability of the cuticular properties, we did not perform extensive anatomy, but instead measured reflectance spectra of several single tiles of the green and purple areas wtih a microspectrometer. We thus found that the reflectance spectra are somewhat variable in both peak wavelength and amplitude. Figure 9 gives a few spectra, normalized for clarity's sake. The reflectance amplitudes of the green and purple areas were rather similar, but varied within a range of a factor 1.5. Presumably, therefore, the layering of the elytra will vary accordingly.

Usually, multilayers are treated as a stack of discrete layers that have an alternating low and high refractive index, n_l and n_h, with thicknesses d_l and d_h, respectively. In the case of a so-called ideal multilayer, the optical path length of the layers is constant, $n_l d_l = n_h d_h$, and for normal incident light, the peak reflectance then is at wavelength $\lambda_{max} = 4 n_l d_l = 4 n_h d_h$ [3,16]. Interestingly, although the layers in figure 8a,b are not discrete but graded, the density profiles have peaks that are sharper than the troughs (figure 8c), so roughly similar to an ideal multilayer where $d_h < d_l$. For the green area of figures 5–7, $\lambda_{max} \approx 520$ nm. Assuming heuristically that $d_l = 82$ nm and $d_h = 78$ nm (so that $d_l + d_h = 160$ nm), this would mean that $n_l = 1.59$ and $n_h = 1.67$. For the purple areas of figures 5–7, $\lambda_{max} \approx 670$ nm. Assuming heuristically that $d_l = 105$ nm and $d_h = 100$ nm (so that $d_l + d_h = 205$ nm), this would mean that $n_l = 1.60$ and $n_h = 1.68$. These refractive index values are similar to those estimated for the green and red areas of the elytra of *C. raja* where for normal light incidence the reflectance peak wavelengths are about 550 and 610 nm. The values $n_l = 1.55$ and $n_h = 1.68$ were obtained by modelling the multilayers as a stack of 16 discrete layers with varying thicknesses [10].

(e) *Modelling*
To improve our insight into the polarization- and angle-dependent reflectance spectra of a multilayer, we have calculated the spectra for an ideal multilayer consisting of 14 layers that maximally reflects normal incident light with wavelength 600 nm (figure 10). We first considered the case that the layers were non-absorbing and had alternating refractive indices $n_l = 1.60$ and $n_h = 1.68$. At the front side, the stack faced the air, with refractive index $n_0 = 1$, and at the end, the refractive index was taken to be $(n_l + n_h)/2$. Figure 10a,c presents the reflectance spectra for TE- and TM-polarized light for angles of incidence, θ_0, increasing in steps of 10°. The peak wavelength, λ_{max}, of the TE spectra decreased with an increasing angle of incidence (blue symbols in figure 10e), as expected from the interference condition $\lambda_{max} = 2 (n_l d_l \cos \theta_l + n_h d_h \cos \theta_h)$, where the angles θ_l and θ_h at the interfaces are determined by Snell's Law: $n_l \sin \theta_l = n_h \sin \theta_h = n_0 \sin \theta_0$ ($\lambda_{max}(\theta_0)$ is given in figure 10e by the green line). The peak wavelengths of the TM light were identical to those of the TE spectra for $\theta_0 < \theta_B = 69.3°$, where θ_B is the generalized Brewster angle [17], but for $\theta_0 > \theta_B$, the spectral shape of the TM spectra was inversed so that then the trough wavelength of TM spectra equalled the peak wavelength of the TE spectra (figure 10e). The amplitude of the TE spectra increased with θ_0 (figure 10a,g), but the amplitude of the TM spectra decreased with θ_0 for $\theta_0 < \theta_B$, and for $\theta_0 > \theta_B$ the amplitude increased again (figure 10c,g).

In the second case considered, the high refractive index layers were absorbing, with imaginary component $k = 0.1$. For both TE- and TM-polarized light, the resulting reflectance spectra showed an enhanced reflectance at the long-wavelength side of the peak (figure 10b,d; see also [9,13]). The peak
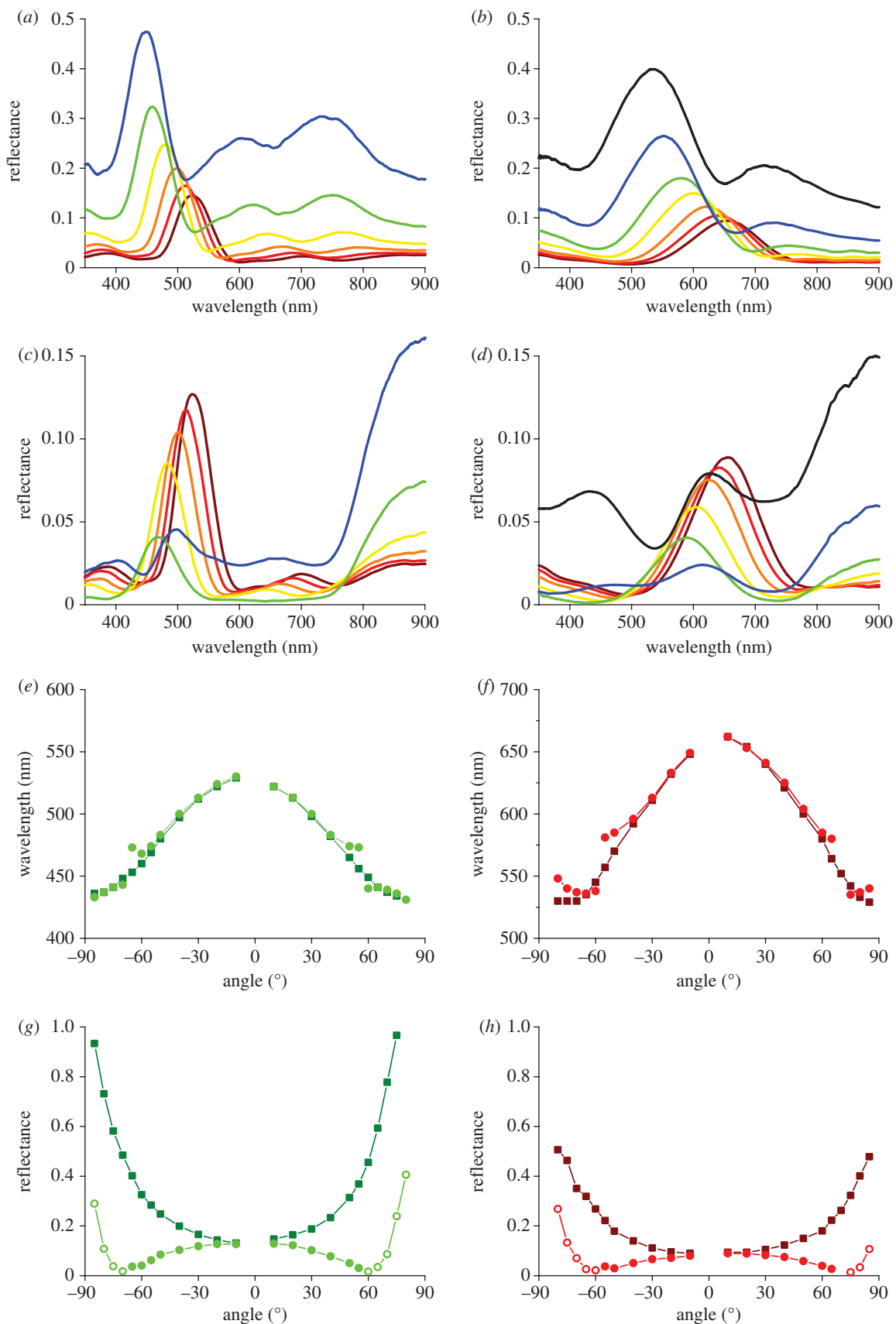
Figure 7. Angle-dependent reflectance spectra for (*a,b*) TE- and (*c,d*) TM-polarized light measured with the fibre optic set-up of figure 2*a* for (*a,c,e,g*) green and (*b,d,f,h*) purple elytral pieces. With an increase in the angle of incidence, the peak wavelength shifted to shorter wavelengths for both TE- and TM-polarized light (*e,f*). The reflectance peak value continuously increased for TE light, but had a biphasic behaviour for TM light (*g,h*). Data points for angles around 0° are lacking, because there the illumination fibre obstructs the reflection measurement. The profiles in (*e*)−(*h*) are not perfectly symmetrical with respect to $\theta_0 = 0°$, because of the slightly non-horizontal elytral surface. Keys: (*a,b,c,d*) brown line, 20°; red line, 30°; orange line, 40°; yellow line, 50°; green line, 60°; blue line, 70°; black line, 80°. (*e,g*) Filled green squares, TE; filled green circles, TM. (*f,h*) Filled red squares, TE; filled red circles, TM.
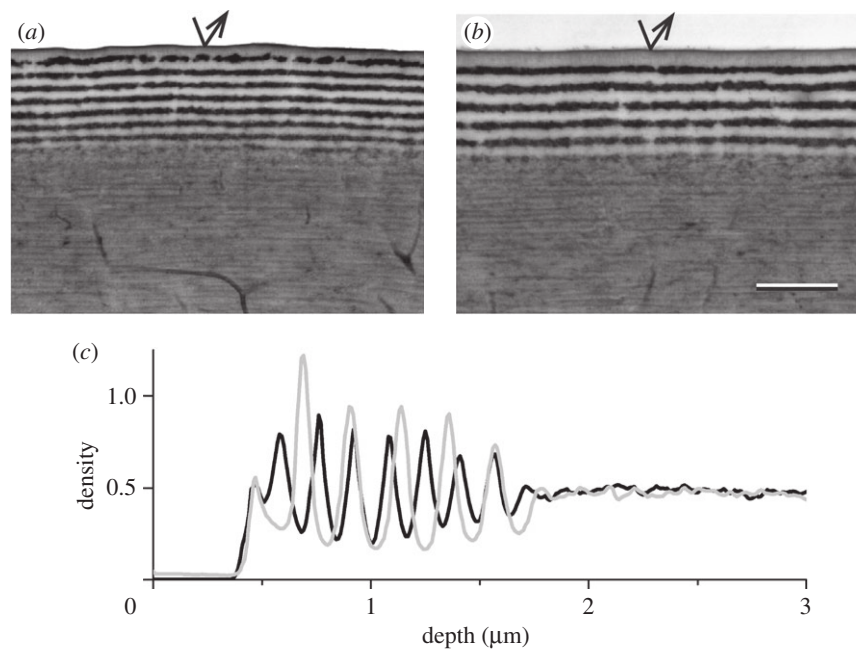
Figure 8. Transmission electron micrograph of (*a*) green and (*b*) purple sections of the jewel beetle elytra (scale bar, 1 µm). The green and purple areas have about 16 and 12 layers, respectively, in the 1.3 µm thick epicuticle. The average optical density calculated in 10 nm thick layers perpendicularly to the surface oscillates more or less sinusoidally as a function of depth (*c*). (*c*) Black line, green; grey line, purple.
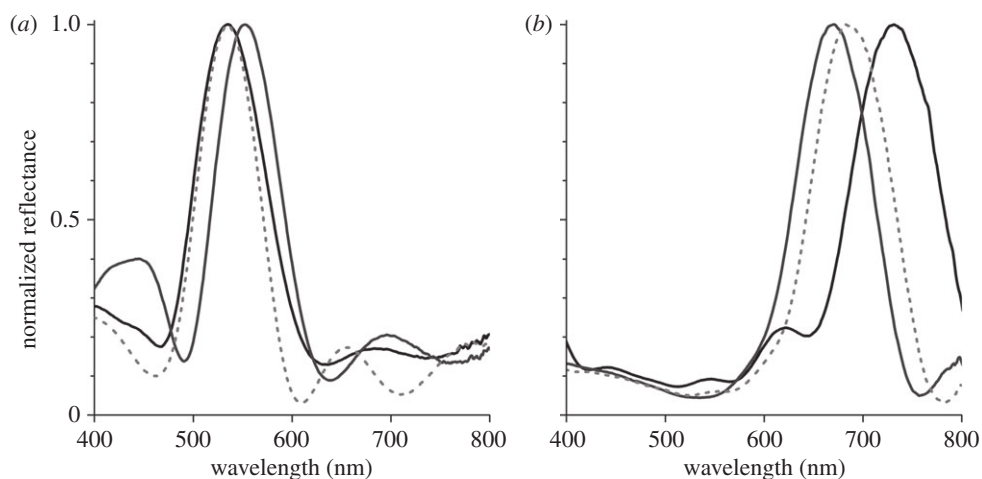

Figure 9. A few normalized reflectance spectra measured microspectrophotometrically from single (*a*) green and (*b*) red/purple elytral tiles.

wavelength as a function of angle of incidence was accordingly slightly bathochromic shifted (figure 10*e*; red line symbols and line). The absorptance spectra associated with the constant k showed a trough where the reflectance spectra had a peak, and outside that wavelength range, the absorptance gradually decreased with increasing wavelength. This was to be expected, because the absorption coefficient, $\alpha(\lambda)$, is related to the imaginary component of the refractive index by $\alpha(\lambda) = 4\pi k/\lambda$.

Transmission measurements of the elytra demonstrated that the absorption decreases much more strongly with wavelength than follows from a constant k. In our further calculations, we therefore have used a wavelength-dependent imaginary component of the refractive index derived from the transmission measurements (figure 11*a*). Furthermore, the graded density of the transmission electron micrographs strongly suggests that treating the beetle epicuticle as a stack of discrete layers with constant refractive indices is a very crude approximation (figure 8*c*). A better approximation presumably is that the refractive index is a function of the derived optical density. This was implemented in a model treating the multilayer as a large stack of thin (10 nm thick) layers with a refractive index, the real and imaginary components of which are linearly proportional to the determined average density. Figure 11*b*,*c* presents the depth profiles of the real and imaginary parts of the refractive index for the green and purple areas that were used in the calculations of the polarization- and angle-dependent reflectance spectra (figure 12*a*,*b*).
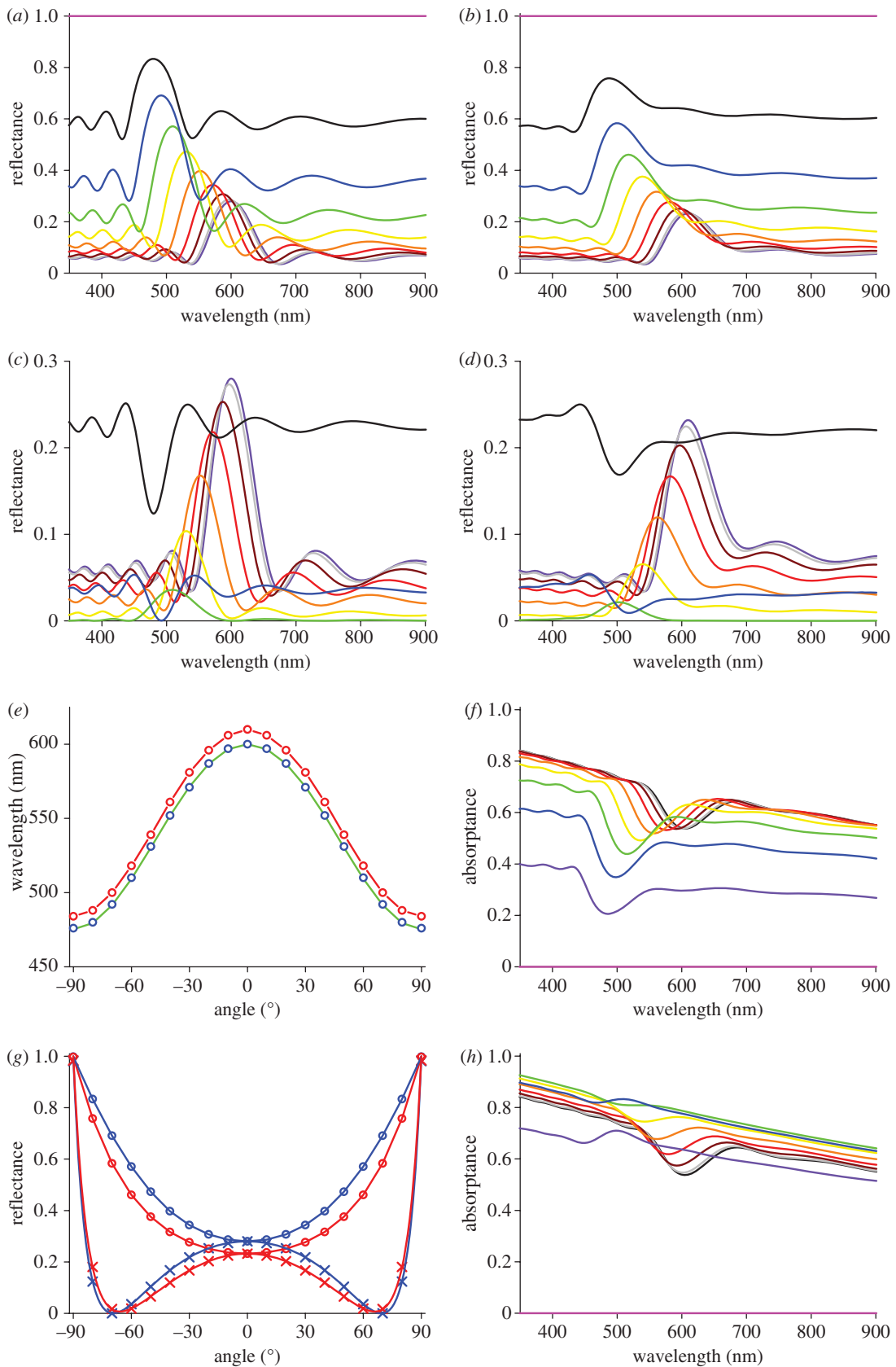
Figure 10. Angle-dependent reflectance and absorptance spectra of an ideal multilayer with peak reflectance at 600 nm for normal incidence light. The (real parts of the) refractive indices of the 14 layers were $n_l = 1.60$ and $n_h = 1.68$. (a,c) Reflectance spectra for angles of incidence increasing in steps of $10°$ in the case of no absorption, that is, the imaginary part of the refractive index is $k = 0$. (b,d) Reflectance spectra when the high refractive index layers absorb light: $k = 0.1$. (e) The reflectance peak wavelength as a function of the angle of incidence for TE-polarized light, for $k = 0$ (blue symbols) together with the prediction of the interference condition (green line), and for $k = 0.1$ (red symbols and line). (g) Reflectance amplitude at the peak wavelength of TE-polarized light, as a function of the angle of incidence for TE light (open symbols) and TM light (crosses). Open blue circles: TE, minus; open red circles: TE, plus; blue crosses: TM, minus; red crosses: TM, plus. (f,h) Absorptance spectra for TE and TM light for the different angles of incidence when $k = 0.1$. Keys: (a,b,c,d,f,h) black line, $0°$; purple line, $80°$; grey line, $10°$; brown line, $20°$; red line, $30°$; orange line, $40°$; yellow line, $50°$; green line, $60°$; blue line, $70°$; pink line, $90°$.
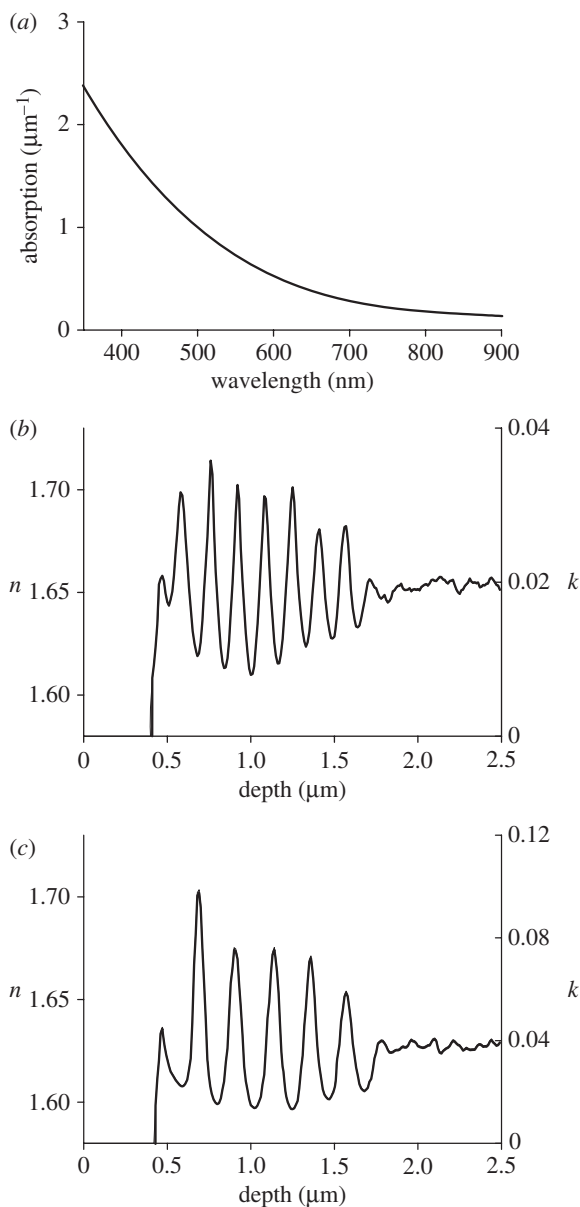
Figure 11. (*a*) Melanin absorption spectrum and refractive index profiles of (*b*) the green and (*c*) purple areas used in the calculations of the reflectance spectra (see §2). The right-hand ordinates in (*b*) and (*c*) represent $k(z, \lambda = 500$ nm).

From these spectra, the angle dependence of the peak wavelength (figure 12*e*) and amplitude (figure 12*f*) were derived. The range of real and imaginary parts of the refractive index was chosen so that the calculated reflectance spectra resembled those for the green area of the experiment of figure 7. The absorptance spectra associated with the calculated reflectance spectra are presented in figure 12*c,d*.

Figure 13 presents the parallel results for the purple area, obtained with the refractive index values of figure 11*c*. Using similar refractive index values as those chosen for the green area produced reflectance spectra with a similar shape as those for the purple area of figure 7, but the peak wavelengths were batho-chromic shifted. Given the local variability in spectral properties (figure 9), we conclude that the TEM section yielding the micrograph of figure 8*b* was from a more deep-red/purple area than that investigated in the reflectance spectra measurements of figure 7*b,d*.

4. DISCUSSION

(a) *The refractive index of melanin in biological tissue*

Reflecting multilayers in insect cuticle have been extensively studied in various beetle species [18–22]. In transmission electron micrographs, the multilayers are recognized as a stack of layers with alternating high and low electron density. The multilayers in the epicuticle of jewel beetles exhibit a strong polarized iri-descence, a well-known property of optical multilayers, which has been amply applied in reflecting polarizers (e.g. [17]). The jewel beetle's multilayers are presum-ably homogeneous, causing only linear polarization, whereas circular polarization is a dominant feature in scarab beetles [18,20,23,24]. For scarab beetles, Caveney [18] concluded that the reflective layers had a high concentration of uric acid, causing a high refrac-tive index value of about 1.70. Durrer & Villiger [5] noticed for the elytra of the buprestid *E. gigantea* that the distribution of the high refractive material was patchy, but without further evidence they stated that the material would be melanin, with a refractive index of 2.0. In their wake, Schultz & Rankin [22] concluded that *Cicindela* tiger beetle cuticle contains melanoprotein producing a refractive index near 2.0. A refractive index value of 2.0 for beetle cuticle is most probably much too high [8,10,19], but we agree with Durrer & Villiger [5] that the material of the cuticular multilayers, probably melanin, is not deposited in discrete layers, as is commonly assumed (e.g. [10,21,25]).

(b) *Refractive index range*

Taking into account that for multilayers the wave nature of light is of predominant importance, we con-cluded that the refractive index profile of a multilayer changes gradually instead of stepwise. The measured reflectance spectra were modelled with refractive index values that varied between 1.60 and 1.70 (figures 12 and 13), where the latter value is similar to the maximal refractive index values derived for scarab beetle cuticle by Caveney [18] and for *C. raja* by Noyes *et al.* [10]. The modelling showed that the peak wavelength and amplitude of the reflectance spectra are quite sensitive for the range of the refractive index. In the presence of absorption, the side bands start to vanish (figure 10*a,b*). Side bands were indeed not prominent in the reflectance spectra measured with the scatterometer and the two-fibre set-up (figures 6 and 7), but distinct side bands were found in the reflectance spectra measured microspec-trophotometrically from individual elytral tiles (figure 9*a*). The spectra measured from neighbouring tiles appeared to vary in amplitude and peak position, and therefore the spectra from areas comprising several tiles would have lost fine structure. We there-fore tentatively conclude that modelling of the spectra from the larger areas overestimates the imagin-ary component of the refractive index. In other words, the absorptance spectra calculated for the epi-cuticle (figures 12*c,d* and 13*c,d*) may be somewhat too large. Given the variability in the experimental spectra and the difficulty of connecting the local
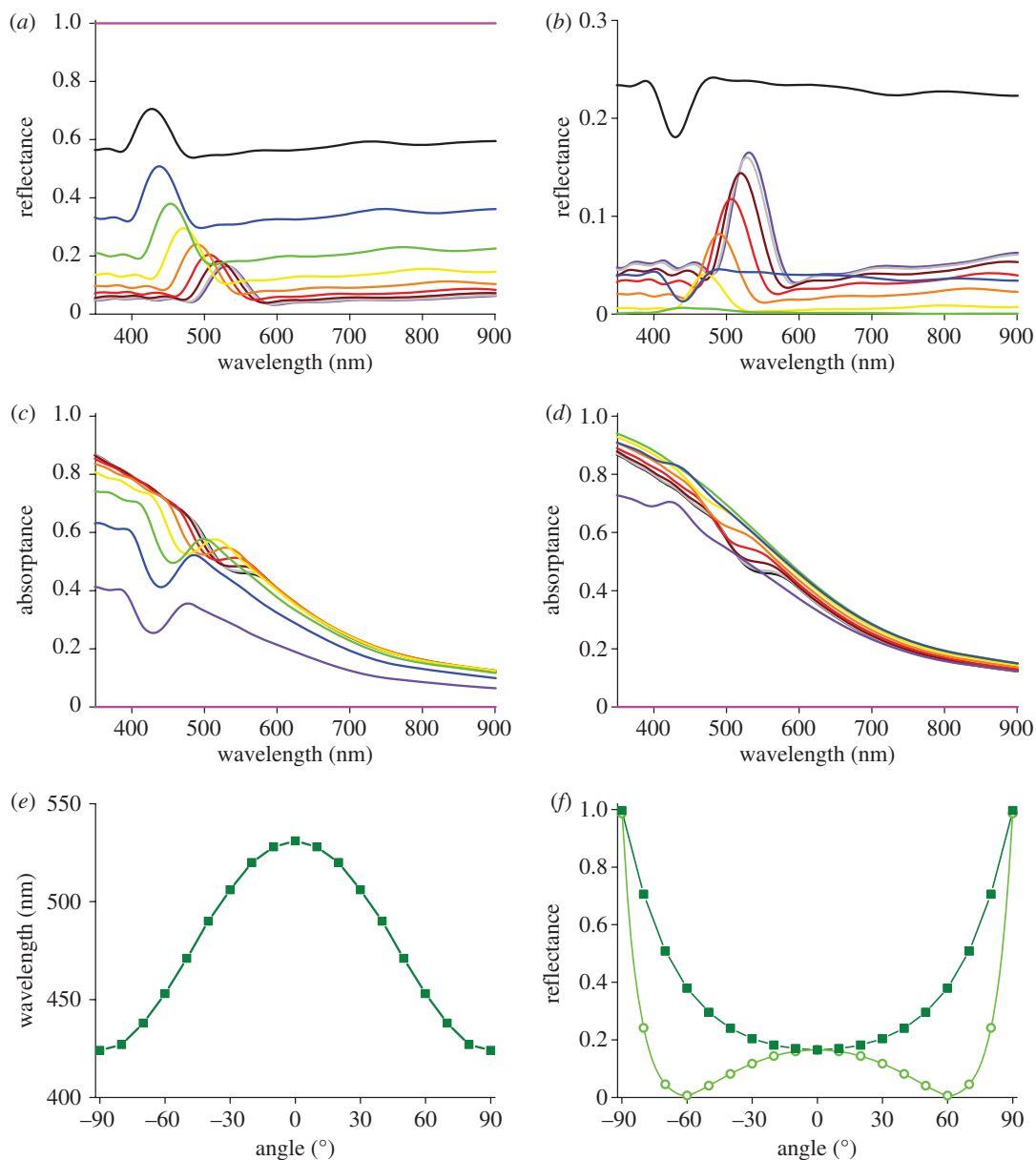
Figure 12. (*a,b*) Reflectance spectra and (*c,d*) absorptance spectra calculated with the multilayer formalism of the appendix using the refractive index values for the green area of figure 11. (*e*) The peak wavelength of TE-polarized light as a function of angle of light incidence following from (*a*) and (*b*). (*f*) Reflectance amplitudes as a function of angle of light incidence of the TE- and TM-light at the peak wavelengths of (*e*). Keys: (*a,b,c,d*) black line, 0°; grey line, 10°; brown line, 20°; red line, 30°; orange line, 40°; yellow line, 50°; green line, 60°; blue line, 70°; purple line, 80°; pink line, 90°. (*e,f*) Filled green squares, TE; open green circles, TM.

anatomy with the spectral properties of the elytra, a fully quantitative treatment is presently impossible. Nevertheless, we expect that the actual profiles of both the real and imaginary parts of the refractive index will not strongly deviate from the present estimates.

(c) **Biological implications**

The range of the refractive index appears to be quite narrow, but with a large stack of 16 (green) or 12 (purple) layers, a bright reflection nevertheless results. In fact, the spectral reflectance values of the jewel beetles are not very different from those of green leaves, which however usually scatter rather diffusely. Female jewel beetles remain stationary, with closed elytra, on leaves or twigs of a host tree when searched

by male jewel beetles [8]. Males can detect a potential female mate from a distance of several metres, but the applied detection criteria have not yet been satisfactorily established. Studies with models constructed from male and female elytra showed that they were equally attractive, but models made from light-emitting diodes with emission spectra similar to those of the elytral reflection spectra were fully unattractive [8]. Imaging scatterometry of the jewel beetle's elytra demonstrated that the light reflected at angles around 60° is highly (linearly) polarized. This will determine the appearance and thus the visibility of the beetles in nature. Polarized reflection patterns appear to be widespread among insects [26,27] and can serve for intraspecific signalling [28]. Our present hypothesis, that the polarized iridescence exhibited
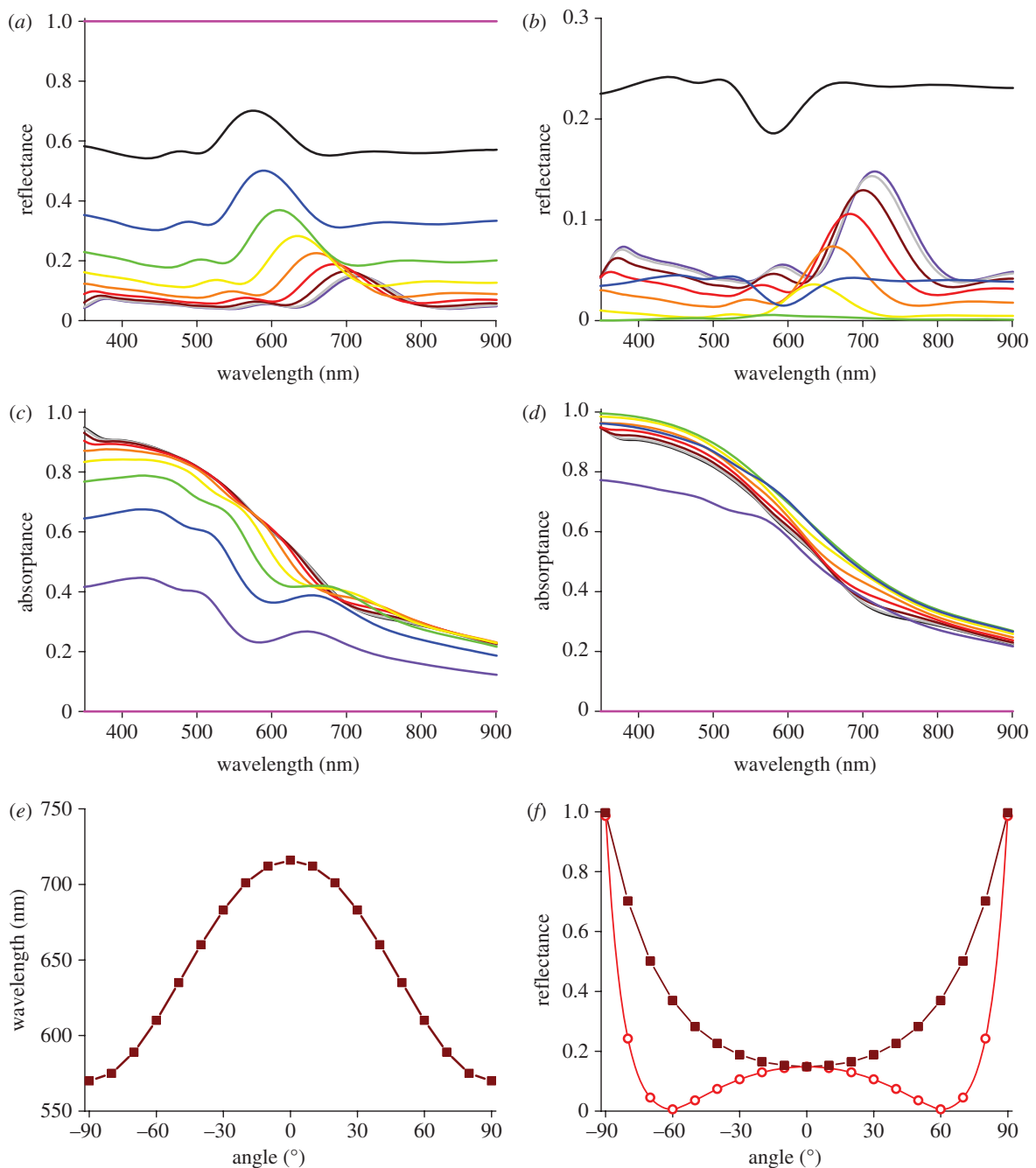
Figure 13. (*a,b*) Reflectance spectra and (*c,d*) absorptance spectra calculated with the multilayer formalism of the appendix using the refractive index values for the red area of figure 11. (*e*) The peak wavelength of TE-polarized light as a function of angle of light incidence following from (*a*) and (*b*). (*f*) Reflectance amplitudes as a function of angle of light incidence of the TE- and TM-light at the peak wavelengths of (*e*). Keys: (*a,b,c,d*) black line, 0°; grey line, 10°; brown line, 20°; red line, 30°; orange line, 40°; yellow line, 50°; green line, 60°; blue line, 70°; purple line, 80°; pink line, 90°. (*e,f*) Filled red squares, TE; open red circles, TM.

by the reflecting elytra provides valuable clues for the presence of a sitting female, will be tested in the near future.

5. CONCLUSIONS

— Using a novel ISM, we visualized the polarization and angle dependence of the striking metallic reflection of the jewel beetle *C. fulgidissima*.
— Quantitative spectral measurements could be well modelled with the classical multilayer theory incorporating absorption by melanin.

— Green and purple stripes are created by a multi-layer that has a surprisingly small gradient refractive index range of 1.6–1.7.
— We conclude that melanin-doped chitin layers have a refractive index of approximately 1.7, significantly lower than the previously assumed value of 2.0.
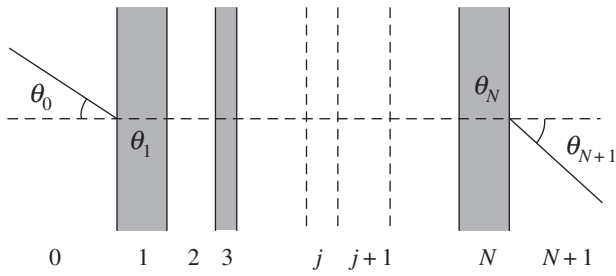
Figure 14. Diagram of light propagation through a multilayer existing of N layers with refractive indices $n_j, j = 1, 2, \ldots, N$, bordered by media with refractive index n_0 and n_{N+1}. The angles of light incidence and refraction at the interface of media j and $j + 1$ are θ_j and θ_{j+1}, respectively.

APPENDIX A: CALCULATION OF THE REFLECTANCE AND TRANSMITTANCE OF A MULTILAYER WITH THE MATRIX FORMALISM

The reflectance and transmittance of a multilayer can be effectively calculated with a matrix formalism describing the propagation of light from layer to layer. Yeh [16] provides a most accessible treatise, which is summarized here and slightly expanded.

We consider a general multilayer consisting of N infinite wide layers of homogeneous dielectric media, separated by parallel surfaces, faced by media with real refractive indices n_0 and n_{N+1} (figure 14). The layer thickness is d_j and the (in general complex) refractive index is $\tilde{n}_j = n_j - ik_j$ $(j = 1, 2, \ldots, N)$; the imaginary part of the refractive index, k_j, is related to the absorption coefficient of the medium, α_j, by $k_j = \alpha_j \lambda / 4\pi$, where λ is the light wavelength. The propagation of light through this multilayer is governed by Snell's Law:

$$\tilde{n}_j \sin \theta_j = n_0 \sin \theta_0, \quad j = 1, 2, \ldots, N + 1,$$

where the angle of incidence θ_j of the light ray at the interface of media j and $j + 1$ can be complex. The light propagation through the multilayer is described by the transfer matrix

$$M = \begin{pmatrix} M_{11} & M_{12} \\ M_{21} & M_{22} \end{pmatrix}$$
$$= D_0^{-1} \left[\prod_{j=1}^{N} D_j P_j D_j^{-1} \right] D_{N+1}, \quad (A\,1)$$

where

$$D_j = \begin{pmatrix} p_j & p_j \\ q_j & -q_j \end{pmatrix}, \quad j = 0, 1, 2, \ldots, N + 1 \quad (A\,2)$$

and

$$P_j = \begin{pmatrix} s_j & 0 \\ 0 & 1/s_j \end{pmatrix}, \quad j = 1, 2, \ldots, N, \quad (A\,3)$$

with $p_j = 1$ and $q_j = \tilde{n}_j \cos \theta_j$ for TE waves, $p_j = \cos \theta_j$ and $q_j = \tilde{n}_j$ for TM waves and $s_j = \exp (i\varphi_j)$, with $\varphi_j = 2/\lambda \, \tilde{n}_j d_j \cos \theta_j$. The reflectance of the multilayer

then is

$$R = \left| \frac{M_{21}}{M_{11}} \right|^2, \quad (A\,4)$$

and the transmittance is

$$T = \frac{n_{N+1}}{n_0} \frac{\cos \theta_{N+1}}{\cos \theta_0} \left| \frac{1}{M_{11}} \right|^2. \quad (A\,5)$$

The computational time needed to evaluate the matrix elements of equation (A 1) can be substantially reduced by realizing that in equation (A 1),

$$D_j P_j D_j^{-1} = \begin{pmatrix} a_j & ib_j p_j / q_j \\ ib_j q_j / p_j & a_j \end{pmatrix}, \quad (A\,6)$$

where $a_j = \cos \varphi_j$ and $b_j = \sin \varphi_j$. Expressions similar to equation (A 6) are given by, for example, Born & Wolf [14], Macleod [15] and Bass [29].

REFERENCES

1 Durrer, H. 1977 Schillerfarben der Vogelfeder als Evolutionsproblem. *Denkschr. Schweiz. Naturforsch. Ges.* **91**, 1–126.
2 Kinoshita, S. 2008 *Structural colors in the realm of nature*. Singapore: World Scientific.
3 Land, M. F. 1972 The physics and biology of animal reflectors. *Prog. Biophys.* **24**, 77–105. (doi:10.1016/0079-6107(72)90004-1)
4 Mason, C. W. 1927 Structural colors in insects. III. *J. Phys. Chem.* **31**, 1856–1872. (doi:10.1021/j150282a008)
5 Durrer, H. & Villiger, W. 1972 Schillerfarben von *Euchroma gigantea* (L.): (Coleoptera: Buprestidae): Elektronenmikroskopische Untersuchung der Elytra. *Int. J. Insect Morphol. Embryol.* **1**, 233–240. (doi:10.1016/0020-7322(72)90031-1)
6 Deparis, O., Vandenbem, C., Rassart, M., Welch, V. L. & Vigneron, J. P. 2006 Color-selecting reflectors inspired from biological periodic multilayer structures. *Opt. Express* **14**, 3547–3555. (doi:10.1364/OE.14.003547)
7 Vigneron, J. P., Rassart, M., Vandenbem, C., Lousse, V., Deparis, O., Biro, L. P., Dedouaire, D., Cornet, A. & Defrance, P. 2006 Spectral filtering of visible light by the cuticle of metallic woodboring beetles and microfabrication of a matching bioinspired material. *Phys. Rev. E* **73**, 041 905. (doi:10.1103/PhysRevE.73.041905)
8 Hariyama, T., Hironaka, M., Takaku, Y., Horiguchi, H. & Stavenga, D. G. 2005 The leaf beetle, the jewel beetle, and the damselfly; insects with a multilayered show case. In *Structural color in biological systems—principles and applications* (eds S. Kinoshita & S. Yoshioka), pp. 153–176. Osaka, Japan: Osaka University Press.
9 Kinoshita, S., Yoshioka, S. & Miyazaki, J. 2008 Physics of structural colors. *Rep. Prog. Phys.* **71**, 076 401. (doi:10.1088/0034-4885/71/7/076401)
10 Noyes, J. A., Vukusic, P. & Hooper, I. R. 2007 Experimental method for reliably establishing the refractive index of buprestid beetle exocuticle. *Opt. Express* **15**, 4351–4358. (doi:10.1364/OE.15.004351)
11 Stavenga, D. G., Leertouwer, H. L., Pirih, P. & Wehling, M. F. 2009 Imaging scatterometry of butterfly wing scales. *Opt. Express* **17**, 193–202. (doi:10.1364/OE.17.000193)
12 Vukusic, P. & Stavenga, D. G. 2009 Physical methods for investigating structural colours in biological systems.

J. R. Soc. Interface **6**(Suppl. 2), S133–S148. (doi:10. 1098/rsif.2008.0386.focus)

13 Wilts, B. D., Leertouwer, H. L. & Stavenga, D. G. 2009 Imaging scatterometry and microspectrophotometry of lycaenid butterfly wing scales with perforated multilayers. *J. R. Soc. Interface* **6**(Suppl. 2), S193–S202. (doi:10. 1098/rsif.2008.0299.focus)

14 Born, M. & Wolf, E. 1975 *Principles of optics*. Oxford, UK: Pergamon Press.

15 Macleod, H. A. 1986 *Thin-film optical filters*. Bristol, UK: Adam Hilger.

16 Yeh, P. 2005 *Optical waves in layered media*. Hoboken, NJ: Wiley-Interscience.

17 Mahlein, H. F. 1974 Generalized Brewster-angle conditions for quarter-wave multilayers at non-normal incidence. *J. Opt. Soc. Am.* 64, 647–653. (doi:10.1364/ JOSA.64.000647)

18 Caveney, S. 1971 Cuticle reflectivity and optical activity in scarab beetles: the rôle of uric acid. *Proc. R. Soc. Lond. B* **178**, 205–225. (doi:10.1098/rspb.1971.0062)

19 Kurachi, M., Takaku, Y., Komiya, Y. & Hariyama, T. 2002 The origin of extensive colour polymorphism in *Plateumaris sericea* (Chrysomelidae, Coleoptera). *Naturwissenschaften* **89**, 295–298. (doi:10.1007/s00114-002-0332-0)

20 Neville, A. C. & Caveney, S. 1969 Scarabeid beetle exocuticle as an optical analogue of cholesteric liquid crystals. *Biol. Rev.* **44**, 531–562. (doi:10.1111/j.1469-185X.1969.tb00611.x)

21 Parker, A. R., McKenzie, D. R. & Large, M. C. J. 1998 Multilayer reflectors in animals using green and gold beetles as contrasting examples. *J. Exp. Biol.* **201**, 1307–1313.

22 Schultz, T. D. & Rankin, M. A. 1985 The ultrastructure of the epicuticular interference reflectors of tiger beetles (*Cicindela*). *J. Exp. Biol.* **117**, 87–110.

23 Goldstein, D. H. 2006 Polarization properties of Scarabaeidae. *Appl. Opt.* **45**, 7944–7950. (doi:10.1364/AO. 45.007944)

24 Sharma, V., Crne, M., Park, J. O. & Srinivasarao, M. 2009 Structural origin of circularly polarized iridescence in jeweled beetles. *Science* **325**, 449–451. (doi:10.1126/ science.1172051)

25 Mossakowski, D. 1979 Reflection measurements used in the analysis of structural colours of beetles. *J. Microsc.* **116**, 351–364.

26 Douglas, J. M., Cronin, T. W., Chiou, T. H. & Dominy, N. J. 2007 Light habitats and the role of polarized iridescence in the sensory ecology of neotropical nymphalid butterflies (Lepidoptera: Nymphalidae). *J. Exp. Biol.* **210**, 788–799. (doi:10.1242/jeb.02713)

27 Stavenga, D. G., Giraldo, M. & Leertouwer, H. L. 2010. Butterfly wing colors: glass scales of *Graphium sarpedon* cause polarized iridescence and enhance blue/green pigment coloration of the wing membrane. *J. Exp. Biol.* **213**, 1731–1739. (doi:10.1242/jeb.041434)

28 Sweeney, A., Jiggens, C. & Johnsen, S. 2003 Polarized light as a butterfly mating signal. *Nature* **423**, 31–32. (doi:10.1038/423031a)

29 Bass, M. 1995 *Handbook of Optics*, vol. 1, 2nd edn. New York, NY: McGraw-Hill.